Dino Düwel, Christoph Otte*, Kevin Schulz, Thore Saathoff, and Alexander Schlaefer

Towards contactless optical coherence elastography with acoustic tissue excitation

Abstract: Elastography presents an interesting approach to complement image data with mechanical tissue properties. Typically, the tissue is excited by direct contact to a probe. We study contactless elastography based on optical coherence tomography (OCT) and dynamic acoustic tissue excitation with airborne sound. We illustrate the principle and an implementation using sound waves of 135 Hz to excite the tissue. The displacement is measured and results of several tests indicate the feasibility to obtain a qualitative measure of the mechanical tissue properties. The approach is interesting for optical palpation, e.g., to enhance navigation and tissue characterization in minimally invasive and robot-assisted surgery.

Keywords: Optical Coherence Tomography; Vibrometry; Elastography; OCE; OCT; Tissue Classification; Mechanical Tissue Properties

DOI: 10.1515/CDBME-2015-0054

1 Introduction

Measuring the mechanical properties of tissue can aid the diagnosis and localization of lesions, e.g., during surgery. For instance, tumor tissue is often stiffer than healthy tissue, and hence palpation is used to detect soft tissue lesion, e.g., in breast or prostate. In principle, the different response of the tissue with respect to an external load is measured. This measurement can be done by imaging and is called elastography [1]. Two widely used elastography modalities are ultrasound and MRI elastography, which each have different merits and drawbacks, e.g., related to the temporal and spatial resolution. Optical coherence elastography is another method to measure and display tissue elastic properties based on optical coherence tomography [2]. OCE allows for a high temporal and spatial resolution and can be implemented in endoscopes and catheter probes. One approach for an OCT based tactile sensor has been shown by Kennedy et al. The authors propose a setup were a translucent layer of compliant silicone is placed on the tissue surface. Applying a defined load through the compliant sensor, the tissue mechanical properties can be displayed in an en face image [3, 4]. However, the proposed method requires the presence of an additional sensor element and is therefore difficult to realize in minimal invasive scenarios. We belive that a non-contact measurement of the local tissue mechanical properties would be advantageous. Air puff devices and focused ultrasound have been proposed to realize non-contact excitation of tissue on a micrometer scale, but usually require a rather sophisticated calibration of the imaging position and excitation hot spot [5, 6]. As an alternative acoustic waves can be transmitted through narrow tubes, thus could be implemented in endoscopic applications [7]. Subhash et al used such an approach to realize a OCT based middle ear vibrometry [8]. We study whether contactless acoustic tissue excitation and OCE can be used to identify differences in tissue elasticity. Our results illustrate that this is feasible and even subsurface variations in mechanical tissue properties can be detected.

***Corresponding Author: Christoph Otte:** Institute of Medical Technology, Hamburg University of Technology, E-mail: christoph.otte@tu-harburg.de

Dino Düwel, Kevin Schulz, Thore Saathoff, Alexander Schlaefer: Institute of Medical Technology, Hamburg University of Technology

2 Methods

Contactless tissue excitation is achieved with a miniature fullrange speaker with 28 mm diaphragm (VISATON GmbH & Co KG, Germany). An acoustic waveguide of 100 mm length is mounted in front of the speaker and tightly sealed. The duct inside the waveguide features a gradually tapering cross section and terminates in a circular port of 3 mm diameter, compare Figure 1. The objective of this waveguide is to generate a point-like acoustic source in the very proximity of the tissue, yet in a controllable and reproducible site. Taking advantage of the inverse-square law governing the distance dependency of sound intensity, this reduces excitation of other system components while maintaining a sufficient intensity to induce measurable tissue vibrations. The speaker is driven with an electrical sine wave of 135 Hz produced by a function generator and reinforced to 1.4 V_{RMS} by an audio amplifier. This excitation frequency was chosen as a multiple of the image rate of the OCT device, which in turn was measured to be 2.7 s^{-1} at the imaging parameters described below.

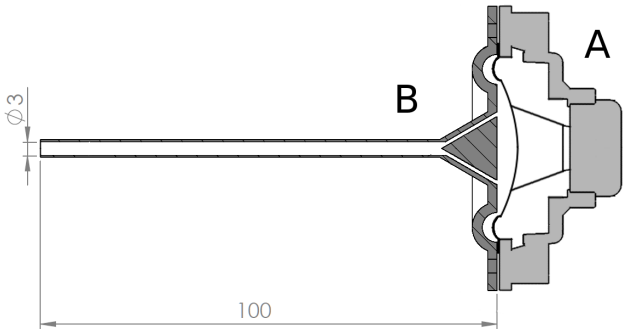

Figure 1: Cross section of the acoustic excitation device consisting of speaker (A) and waveguide (B).

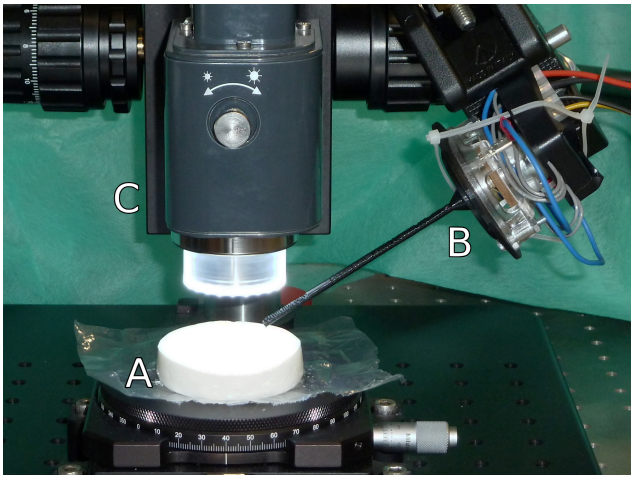

Figure 2: Photograph of the set-up. A: tissue-mimicking phantom, B: waveguide, C: OCT probe.

Spatially resolved phase data is acquired with a *TELESTO* fourier domain OCT device (Thorlabs Inc.) utilizing a super luminescent diode with 1325 nm central wavelength and 150 nm bandwith as the source of low coherence light. The OCT system is characterized by an axial resolution of 6.5 µm in air over a depth range of 2.5 mm and a lateral resolution of 15 µm over a field of view of 10 mm x 10 mm. To obtain a time and depth-resolved phase image (M-scan), 2000 subsequent line scans, each consisting of 512 raw data points distributed over the depth range are acquired and further reduced to an array of 999 by 255 relative phase values, representing the phase shift in adjacent data points due to tissue motion. To reduce phase noise originating from the spectrometer, five subsequent M-scans are averaged and exported to Matlab (The MathWorks, Inc.). The depth-resolved amplitude of phase differences at the excitation frequency, being the representation of acoustically induced tissue motion is then extracted by row wise application of the FFT algorithm.

The experimental set-up can be subdivided into three functional blocks, which are depicted in Figure 2. Four different tissue mimicking gelatin phantoms have been used to perform the experiments. Phantom A and B are equally shaped discs with a diameter of 55 mm, a height of 10 mm and a weight of 40 g. Both phantoms differ in their gelatin concentrations to archive different elastic properties. While the hard phantom contains 6 g of gelatin, phantom B contains only 2 g of gelatin. Phantom C is made from the same low-modulus gelatin concentration as phantom B but contains a spherical inclusion of high-modulus silicone rubber with a diameter of 20 mm centrally located inside the phantom with its highest point resting approx. 3 mm under the upper surface. Phantom D is a cube of 1 cm and consists of three upright layers, with the outer ones being made from the low-modulus gelatin and the inner one of the high-modulus gelatin. The gelatin material of all three phantoms is mixed with a small amount of TiO_2 to ensure sufficient incident light scattering inside the phantom for reliable phase data acquisition.

A total of 40 individual measurements from different sites on hard phantom A (N=20) and soft phantom B (N=20) were taken and processed to yield the same amount of data sets of depth resolved vibrational displacement amplitudes at the excitation frequency. A mean value for the first 100 data points lying below the surface was then calculated for each measurement to further reduce each data set to a single value.

Additionally, measurements of the inclusion phantom C and layered phantom D were taken while laterally scanning the low coherent light beam over a 1 cm long line on the surface, with help of the integrated galvanometer driven mirror scanner. Thus, a spatially resolved phase image (B-scan) is acquired. B-Scans of phantom D were collected from lines directly located over the silicone sphere, as well as from lines not over the inclusion for reference. Multiple B-Scans from adjacent lines on phantom D were acquired to obtain an en face phase image.

To retain the transverse spatial resolution in the discrete frequency transform, a different approach for frequency extraction is chosen in the form of a two-dimensional cross-correlation of the phase image with a (24x48)-convolution kernel, where all rows of the kernel contain a sine wave of the excitation frequency. The resulting cross-correlated signal is then smoothed with a rectangular average filter to account for its periodicity, compare Figure 3.

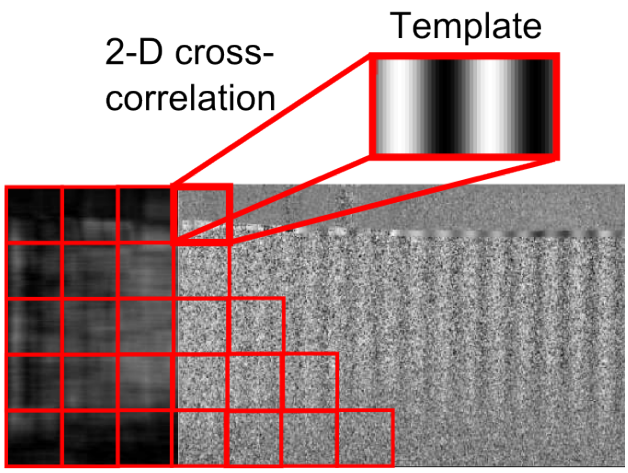

Figure 3: Principle of vibration detection via cross-correlation. The kernel represents the expected excitation frequency and in used to uncover the spatio-temporal motion pattern when scanning.

3 Results

Figure 4 shows the relation between speaker voltage and the displacement. From 0 V to 1.5 V the characteristic appears partially linear with an increasing slope at approximately 1 V. For voltages higher than 1.5 V the characteristic becomes non-linear and the slope decreases to nearly zero. The two groups of mean vibrational amplitudes from

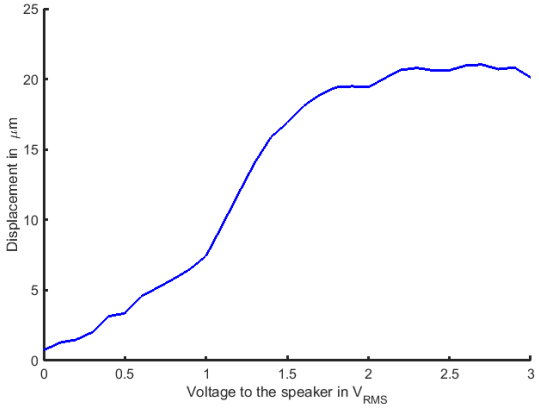

Figure 4: Mean displacement of a hard gelatin Phantom with increasing speaker voltage.

the two homogenous gelatin phantoms were confirmed to both have normal distributed values. The overall mean of vibrational displacement for all points below the surface averaged are 16.1 µm (s=5.3 µm) for the hard phantom A and 36.7 µm (s=6.6 µm) for the soft phantom B. A two-sample t-test assuming unequal variances between groups was performed and revealed a highly significant difference between groups (P<0.001). The depth resolved mean vibrational displacements of both groups are depicted in Figure 5. As for the measurements of the phantom C, which

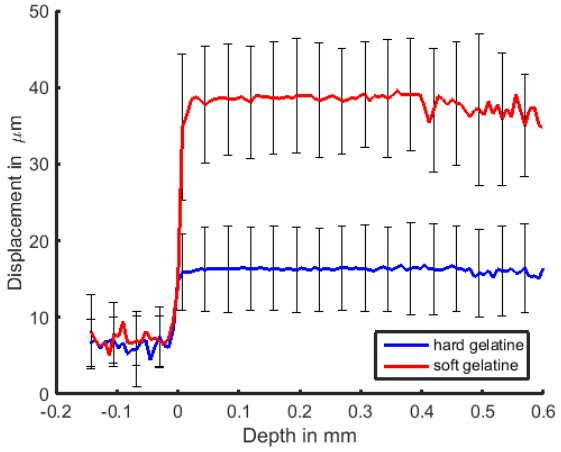

Figure 5: Mean displacement over depth profiles with standard deviation for 20 measurements each of hard and soft gelatin phantom A and B

features a spatially varying modulus, the cross-correlation map was plotted directly and inspected visually. Two of these are shown in Figure 6. The attenuation of the acoustically induced vibration due to the lower elasticity of the underlying inclusion in the upper image can be clearly distinguished in comparison to the reference image below.

The en face displacement maps of the layered phantom D were to be gained by averaging depth resolved correlation coefficients and thereby reducing each of the 25 B-scans to a two-dimensional measure of transverse spatial resolved, acoustically induced tissue displacement. Those were then plotted side by side in a log scaled, color coded en face image, depicted in Figure 7.

4 Discussion

The results indicate that an OCT based elastography with acoustic excitation can help to distinguish tissues with different elastic properties. The relation between the axial displacement and the amplitude of the input signal appears partially linear, but shows a non-linear behavior for

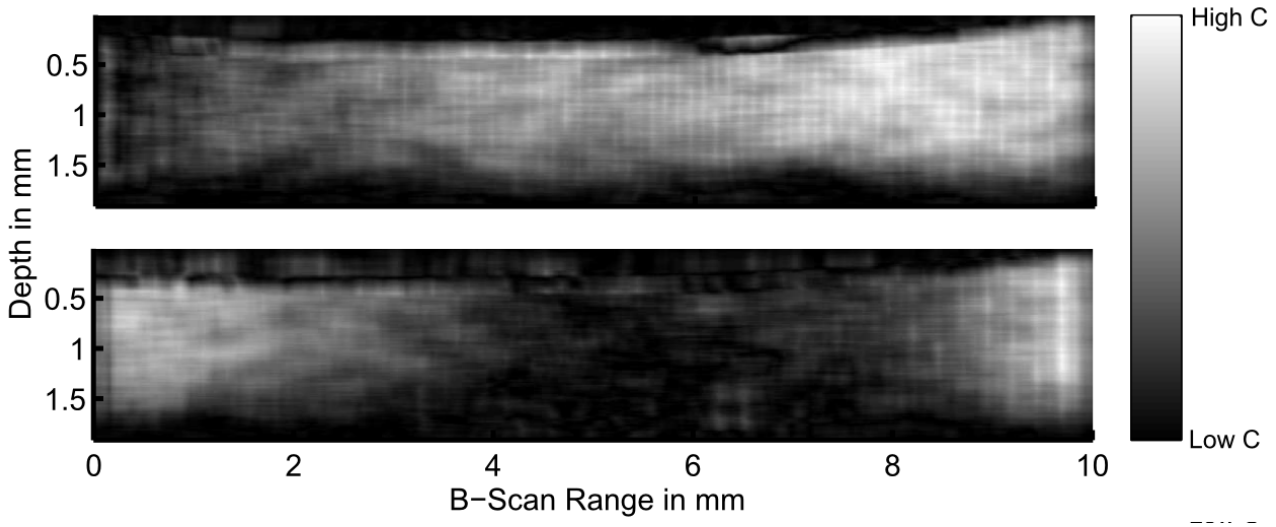

Figure 6: Spatial distribution of 2-D cross correlation coefficient between the phase distribution and a kernel consisting of the reference signal.

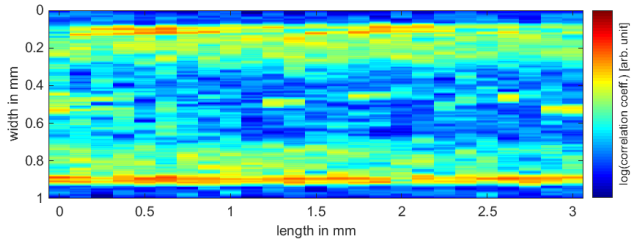

Figure 7: En face image of layered phantom D

higher signal amplitudes. This is probably due to a saturation of the amplifier or a collision of the speaker membrane with the adapter for the waveguide. The detection limit due to phase wrapping or fringe washout of the OCT signal is not reached in this scenario [9]. The spherical inclusion, which is located beneath the imaging range of the OCT has a high influence on the displacement of the tissue on the surface. An analog result was shown in [3, 4] and emphasizes the qualitative nature of the elasticity measurement. Currently the tissue was excited with a single frequency of 135 Hz. However, it has been shown that a frequency depended measurement could provide additional information [10]. Furthermore investigations regarding the optimal application of the acoustic radiation are planned.

Funding: This work was partially supported by DFG grant SCHL 1844/2-1.

Author's Statement

Conflict of interest: Authors state no conflict of interest. Material and Methods: Informed consent: Informed consent has been obtained from all individuals included in this study. Ethical approval: The research related to human use has been complied with all the relevant national regulations, institutional policies and in accordance the tenets of the Helsinki Declaration, and has been approved by the authors' institutional review board or equivalent committee.

References

[1] Parker KJ, Doyley MM, Rubens DJ. Imaging the elastic properties of tissue: the 20 year perspective. Phys. Med. Biol.2011; 56: R1-R29

[2] Chin L, Kennedy BF, Kennedy KM, et al. Three-dimensional optical coherence micro-elastography of skeletal muscle tissue. Biomed Opt Express. 2014; 5(9): 3090–102.

[3] Kennedy KM, Es'haghian S, Chin L, McLaughlin RA, Sampson DD, Kennedy BF. Optical palpation: optical coherence tomography-based tactile imaging using a compliant sensor. Opt Lett. 2014; 39(10): 3014–7.

[4] Es'haghian S, Kennedy KM, Gong P, Sampson DD, McLaughlin RA, Kennedy BF. Optical palpation in vivo: imaging human skin lesions using mechanical contrast. J Biomed Opt. 2015; 20(1): 16013.

[5] Qi W, Li R, Ma T, et al. Resonant acoustic radiation force optical coherence elastography. Appl Phys Lett. 2013; 103(10): 103704.

[6] Wang S, Larin KV. Noncontact depth-resolved micro-scale optical coherence elastography of the cornea. Biomed Opt Express. 2014; 5(11): 3807–21.

[7] Subhash HM, Nguyen-Huynh A, Wang RK, Jacques SL, Choudhury N, Nuttall AL. Feasibility of spectral-domain phase-sensitive optical coherence tomography for middle ear vibrometry. J Biomed Opt. 2012; 17(6): 060505.

[8] Yazaki T, Tashiro Y, Biwa T. Measurements of sound propagation in narrow tubes. Proc. R. Soc. London, Ser. A. 2007; 463: 2855–2862.
[9] Hendargo HC, McNabb RP, Dhalla AH, Shepherd N, Izatt JA. Doppler velocity detection limitations in spectrometer-based versus swept-source optical coherence tomography. Biomed Opt Express. 2011; 2(8): 2175–88.
[10] Adie SG, Liang X, Kennedy BF, John R, Sampson DD, Boppart SA. Spectroscopic Optical Coherence Elastography. Opt Express. 2010; 18(25): 25519-25534.